

Electrical evaluation of the alternating spin current generated via spin-vorticity couplingShoma Tateno,¹ Genki Okano,¹ Mamoru Matsuo,^{2,3,4} and Yukio Nozaki^{1,5}¹*Department of Physics, Keio University, Yokohama 223-8522, Japan*²*Kavli Institute for Theoretical Sciences, University of Chinese Academy of Sciences, No. 3, Nanyitiao, Zhongguancun, Haidian District, Beijing 100190, China*³*RIKEN Center for Emergent Matter Science, Wako, Saitama 351-0198, Japan*⁴*Advanced Science Research Center, Japan Atomic Energy Agency, Tokai, 319-1195, Japan*⁵*Center for Spintronics Research Network, Keio University, Yokohama 223-8522, Japan* (Received 18 February 2020; revised 22 July 2020; accepted 20 August 2020; published 3 September 2020)

In many interacting-electron systems, the microscopic spin angular momentum of electrons is conserved along with the macroscopic angular momentum in electrical current flows, i.e., vorticity. Such spin-vorticity coupling expands the choice of materials for spintronics devices. In this paper, we evaluate the magnitude of an alternating spin current generated by the spin-vorticity coupling with a gigahertz-order surface acoustic wave in a Cu thin film. We measure the gigahertz alternating spin current by an electrical method based on the inverse spin-Hall effect. From the amplitude of the spin current, we can determine the conversion efficiency of the angular momentum between local lattice rotation and electron spin in the Cu film. The conversion efficiency is four orders of magnitude larger than the case of spin current generation via kilohertz-order vorticity in turbulent flow of liquid mercury [M. Matsuo *et al.*, *Phys. Rev. B* **96**, 020401(R) (2017)]. Such a huge conversion efficiency is attributable to a smaller inconsistency of energy scale between lattice rotation and electron spin than the case of liquid vorticity.

DOI: [10.1103/PhysRevB.102.104406](https://doi.org/10.1103/PhysRevB.102.104406)**I. INTRODUCTION**

Spin-vorticity coupling (SVC), which arises when local rotational motions induce an inertial effect in the electron spin, can produce a spin current (SC) in nonmagnetic metals lacking strong spin-orbit interactions (SOIs) [1,2]. SC generation via SVC was first detected in the vorticities of turbulent liquid-mercury flow in a tube [3]. In this early experiment, the temporally uniform component of SC along the radial direction of the tube was measured as a longitudinal direct current (DC) voltage via the inverse spin-Hall effect (ISHE). The SC amplitude is proportional to the flow vorticity [3], suggesting that SVC can be exploited in practical spintronics devices. Matsuo *et al.* theoretically predicted that an alternating SC can be produced by a rotating lattice in elastic solids, e.g., a Rayleigh-type surface acoustic wave (RSAW) [1,4]. The vorticity gradient of the lattice deformation creates a spin-dependent force field which leads to temporally varying spin accumulation and consequent alternating SC. Indeed, Kobayashi *et al.* successfully demonstrated spin wave resonance (SWR) in a NiFe/Cu bilayer by injecting a RSAW with a fundamental frequency of 1.6 GHz [5]. The SWR was strongly suppressed by inserting a SiO₂ insulating layer between the NiFe and Cu and/or by removing the Cu, suggesting that SWR requires the spin-transfer torque (STT) generated by the alternating SC in Cu. SC generation via SVC of the RSAW is advantageous from a technological viewpoint because it is not limited to ferromagnets or noble

metals with a strong SOI but is achievable in a wide range of materials.

A generalized expression of the SC produced via SVC has been deduced by solving a spin diffusion equation with a SVC-related source term which is theoretically predicted by a coarse graining of the collision term in the spin-dependent Boltzmann equation [2]. The deduced SC expression includes a parameter that represents the conversion efficiency of angular momentum from the vorticity field of the lattice to electron spins. The parameter is expressed by the correlation of the vorticity fields using the nonequilibrium density matrix in the presence of the lattice motion. However, it is generally difficult to determine within a theoretical framework because the density matrix reflects the details of the nonequilibrium system consisting of vorticity fields and electron spins as well as a variety of relaxation processes in a realistic situation. To unlock the underlying physics of the angular momentum transfer mechanism in SVC, one must quantitatively evaluate the RSAW-related SC, which is often accompanied by the attenuation of stimulating a RSAW. One might expect that the SC amplitude is easily evaluated from the attenuation of a RSAW owing to the SWR excited via SC application. Indeed, we have experimentally demonstrated the SAW-related SC generation from the SAW attenuation measured by a vector network analyzer [5]. However, the RSAW attenuation in the practical device is generally associated with multiple influences of the electromechanical coupling between the RSAW antenna and the piezoelectric substrate, the acoustic

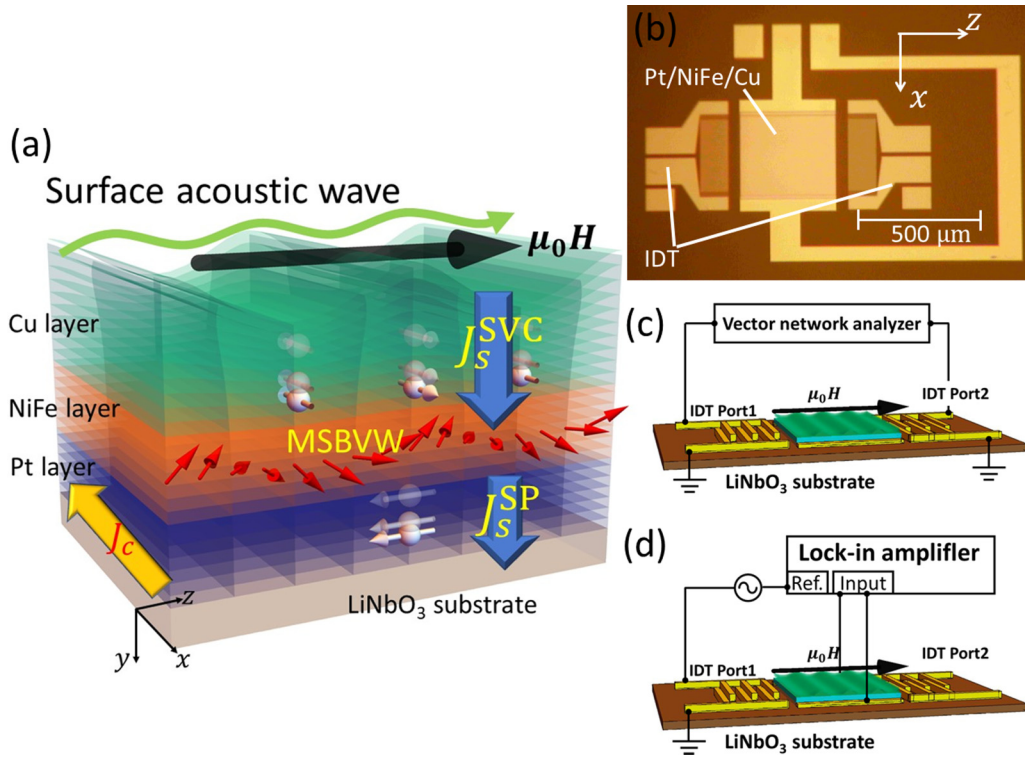


FIG. 1. (a) Geometry of the sample fabricated for measuring the alternating SC generated by applying a RSAW to a Pt/NiFe/Cu trilayer deposited on a LiNbO₃ substrate. The RSAW propagates along the z axis while an external magnetic field $\mu_0 H$ is also applied along the z axis. The SVC with the RSAW propagated in the Cu produces alternating SC J_s^{SVC} along the y axis, which leads to a MSBVW in the NiFe. The spin pumping from the MSBVW generates a direct SC J_s^{SP} in the Pt and consequent Hall voltage along the x axis via ISHE. (b) Optical photograph of the device. The device consists of a pair of IDTs, the Pt/NiFe/Cu trilayer, and an electrode for measuring the Hall voltage. Experimental setups for measuring (c) the RSAW attenuation induced by the SWR and (d) the Hall voltage caused by the spin-pumping effect at the NiFe/Pt interface.

impedance mismatch appearing in the RSAW injection to a metallic thin film, and the multiple scattering of the RSAW.

In this paper, to avoid the influence of such complicated RSAW dissipation on the SC evaluation, we developed an electrical method that directly evaluates the SC using conventional ISHE [6–10], which was widely used to measure SC in many spintronics devices. When a RSAW propagates through trilayer Pt/NiFe/Cu, the SVC produces an alternating SC in Cu, thereby generating a STT on the NiFe magnetization [see Fig. 1(a)]. The temporally and spatially varying STT excites spin waves in NiFe and subsequently generates a direct SC in Pt via the spin-pumping effect [11–13]. The strength of this STT can be evaluated by measuring the voltage appearing in the Pt layer via the ISHE, using an analytical model well established for SWR and spin pumping. One might consider that the alternating SC in the Cu film can be measured simply without inserting a ferromagnetic NiFe film between Cu and Pt. The polarity of the Hall voltage produced via the ISHE of the alternating SC is periodically varied with the wavelength of the RSAW. Consequently, most of the Hall voltage appearing in the Pt is compensated, and the tiny remaining Hall voltage can be measured. For example, when the RSAW with a wavelength of $2.4 \mu\text{m}$ propagates at the Pt/Cu bilayer with a lateral size of $400 \mu\text{m}$, the uncompensated Hall voltage is produced in the portion with a width of $0.8 \mu\text{m}$ ($= 2.4 \mu\text{m} \times 167 - 400 \mu\text{m}$). In this

case, the amplitude of the uncompensated Hall voltage expected from the amplitude of the alternating SC in the Cu is only a few microvolts. Such a tiny alternating Hall voltage is hard to separate with a signal owing to electromagnetic field leakage from the interdigital transducer used to excite the RSAW.

In this study, we explicitly show that the spin pumping from spin waves produces a uniform DC Hall voltage similar to the conventional case driven by uniform precession of magnetization. Thus, we can evaluate the spatially modulated alternating SC which drives SWR by measuring the DC Hall voltage generated in the whole Pt/NiFe/Cu trilayer film. From the amplitude of SC via SVC, we found that the conversion of angular momentum between the electron spin and mechanical vorticity was four orders of magnitude larger than in the case of liquid-mercury flow.

The remainder of this paper is organized as follows. Section II is the theoretical perspective of spin current generation via SVC. Section III describes the experimental setup, and Sec. IV presents the experimentally determined spin-Hall voltage and SWR absorption measurements in the RSAW-injected Pt/NiFe/Cu trilayer. Section V derives the analytical expression for the spin-pumping effect caused by the SWR excitation in NiFe and the subsequent ISHE in Pt. The alternating SC is determined from the spin-Hall voltage by the analytical model in Sec. VI. The paper concludes with Sec. VII.

II. THEORY OF SPIN CURRENT VIA SVC

SVC is defined by the following Hamiltonian [14]:

$$H_{\text{SVC}} = -\frac{\hbar}{4} \boldsymbol{\sigma} \cdot \boldsymbol{\Omega}, \quad (1)$$

where \hbar is the reduced Planck constant and $\boldsymbol{\sigma}$ is the Pauli matrix. $\boldsymbol{\Omega}$ is vorticity given by $\boldsymbol{\Omega} = \nabla \times (\partial \mathbf{u} / \partial t)$, where \mathbf{u} is the vector of the lattice deformation. SVC generates spin-dependent force and creates spin accumulation $\delta\mu$. Considering a spin accumulation owing to the collision of electron spins in the mean field of many-body system with macroscopic vorticity, the spin accumulation meets the spatial and temporal spin-diffusion equation as follows [1,2]:

$$\left(\frac{\partial}{\partial t} - D\nabla^2 + \frac{1}{\tau_{\text{sf}}} \right) \delta\mu = -\frac{\hbar}{\tau_{\text{sf}}} \zeta \Omega_x, \quad (2)$$

where D is the diffusion coefficient and τ_{sf} is the spin-flip time. Ω_x is the x component of vorticity. Here, ζ is a renormalization factor which is originated from the coarse-graining procedure of the lattice motion and represents the conversion efficiency of angular momentum from lattice into electron spins. When a RSAW propagates at the surface of a semi-finite elastic body, the vorticity is given by [1]

$$\Omega_x = \frac{\omega^2 u_0}{c_t} e^{-k_t y} e^{i(kz - \omega t)}. \quad (3)$$

ω and u_0 are the angular frequency and deformation amplitude of the RSAW, respectively. c_t is the transverse velocity of the RSAW. The transverse wave number k_t is given by $k_t = k\sqrt{1 - \xi^2}$, where ξ is given by $\xi \approx (0.875 + 1.12\nu)/(1 + \nu)$ with Poisson ratio ν . k is the wave number of the RSAW. Because the gradient of Ω_x along the y axis is nonzero, the SC, which is proportional to the spatial gradient of $\delta\mu$, propagates along the y axis. The asymptotic solution of Eq. (2) for $k_t y \ll 1$ is described as follows:

$$J_s = \zeta J'_s e^{i(kz - \omega t)} \quad (4)$$

and

$$J'_s \approx \frac{\hbar \sigma_0 \omega^3 u_0}{e c_t^2} \left(1 + \frac{k_t^2 \lambda_s^2}{1 - \xi^2} \right)^{-1/4} \frac{\sqrt{1 - \xi^2}}{\xi} \frac{y}{\lambda_s}, \quad (5)$$

where λ_s and σ_0 are the spin diffusion length and the electrical conductivity, respectively. From Eqs. (4) and (5), it is obvious that the SC is in proportion to σ_0 . This is because a highly conductive Cu has been chosen for the SC generator via SVC of the RSAW.

III. EXPERIMENTAL SETUP

A RSAW device comprising a pair of Ti(3)/Au(30) interdigital transducers (IDTs) with a finger width of 500 nm was fabricated on a 128°-rotated Y-cut LiNbO₃ substrate. When AC voltage is applied to the IDT, a lattice deformation of the substrate periodically arises due to the piezoelectric effect, and elastic vibration propagates on the substrate. In the case of 128°-rotated Y-cut LiNbO₃ substrate, both longitudinal and transverse components of displacements coexist, although those phases differ by $\pi/2$. Consequently, an elliptical oscillation of the lattice, i.e., the RSAW mode,

appears. For all structures given in this paper, the numbers in parentheses are the layer thicknesses in nanometers. As shown in Fig. 1(b), a $400 \times 400 \mu\text{m}^2$ square comprising a Pt(10)/NiFe(20)/Cu(200) trilayer was deposited between the IDTs, where NiFe represents the Ni₈₁Fe₁₉ alloy. The stacking order was LiNbO₃ substrate/Pt/NiFe/Cu, as schematically shown in Fig. 1. To distinguish the SVC-related phenomena from the spin-orbit coupling (SOC)-related one, we chose Cu as a SC generator because its SOC is negligible and the electrical conductivity is almost the highest in metals. The latter property is preferred to improve the SVC, as shown in Eq. (5). An electrode for measuring the Hall voltage along the x axis was also fabricated. All electrodes were fabricated by the conventional liftoff technique using electron-beam lithography and ultrahigh-vacuum evaporation. The trilayer was sputtered at an Ar pressure of 0.22 Pa with a background pressure of approximately 3.0×10^{-4} Pa. Figure 1(a) schematizes the Pt/NiFe/Cu trilayer in which a RSAW generates an alternating SC and the Cartesian coordinates of the system. When a RSAW propagates along the z axis of the trilayer, the vorticity generated toward the x axis accumulates spin in the Cu via SVC. In the device, we can adopt a free-surface condition for the RSAW excitation. The boundary conditions, $\sigma_{xy}|_{\text{surface}} = 0$, $\sigma_{yy}|_{\text{surface}} = 0$ and $\sigma_{zy}|_{\text{surface}} = 0$, where σ_{ij} is the (i, j) component of the stress tensor, determine the distribution of RSAW vorticity in the trilayer as Eq. (3). Thus, the amplitude of RSAW vorticity becomes maximum at the surface of the trilayer film and decays exponentially along the y axis. The spin accumulation gradient in the nonuniform vorticity field generates an alternating SC J_s^{SVC} along the y axis in the Cu film. The SC produces a STT in NiFe, which excites a spin wave in the resonant field $\mu_0 H$. The spin polarization $\boldsymbol{\sigma}$ of the SC varies its sign along the RSAW propagating direction with a period of the RSAW wavelength. Namely, STT on NiFe magnetization, which is given by $\mathbf{m} \times (\mathbf{m} \times \boldsymbol{\sigma})$, also changes periodically. Consequently, the periodic STT excites a magnetostatic backward volume wave (MSBVW), where the wave vector is parallel to the equilibrium direction of magnetization. As schematically shown in Fig. 1(a), the rotation direction of precession is uniform in the whole NiFe layer, although the rotation phase changes periodically because the rotation direction depends on the polarity of external magnetic field along the z axis. Finally, a DC spin current J_s^{SP} is generated in the adjacent Pt via the spin-pumping effect, and voltage induced by the ISHE appears along the x axis. The DC component of SC generated via the spin-pumping effect depends on the magnetization component parallel to the precession axis [15]. The DC Hall voltage therefore uniformly appears in the whole Pt layer, although the phase of precession propagates along the wave vector of the RSAW. The analytical expression of the DC Hall voltage is shown in Sec. V. Figure 1(b) is a photograph of the fabricated device. The experimental setups for measuring microwave absorption and the Hall voltage caused by the SWR excitation are schematized in Figs. 1(c) and 1(d), respectively. We compared the results of two experiments. Similar to Kobayashi *et al.* [5], we first measured the RSAW attenuation under SWR excitation in NiFe by a vector network analyzer (VNA) in the frequency-domain mode [Fig. 1(c)]. The SWR

excitation induced by the alternating SC is responsible for the energy dissipation related to magnetization damping in NiFe. In other words, part of the RSAW energy is diverted into the magnetization dynamics, resonantly reducing the RSAW amplitude. The RSAW-amplitude reduction was evaluated from the S_{21} parameter measured by the VNA in a given static magnetic field [Fig. 1(c)]. In the second experiment, we measured the Hall voltage by the conventional lock-in technique while the RSAW propagated through the trilayer. During the Hall voltage measurement, an IDT transmitter was injected with a pulse-modulated microwave whose frequency was matched to the SWR frequency. The frequency of the pulse modulation was fixed at 188 Hz. The microwave amplitude was set to be 17 dBm. For comparison, we conducted similar experiments on other samples with different layer configurations, namely, LiNbO₃/W(10)/NiFe(20)/Cu(200), LiNbO₃/Pt(10)/SiO₂(20)/NiFe(20)/Cu(200), and LiNbO₃/Pt(10)/NiFe(20)/SiO₂(20)/Cu(200). There are several possibilities of exciting SWR in NiFe other than J_s^{SVC} from the Cu layer. First, we discuss how the magnetic rectification effect in NiFe influences the Hall voltage along the x axis. The electromagnetic-field leakage from the transmitting IDT electromagnetically induces an alternating charge current in the trilayer. Moreover, the magnetization precession in NiFe caused by the RSAW injection leads to a temporal variation in the electrical resistance via the anisotropic magnetoresistance effect. This variation induces a rectified voltage whose magnitude depends on the relative phase difference between the induced alternating charge current and the resistance oscillation. The sign of the magnetic rectification effect in NiFe was independent of the sign of the spin-Hall angle of the nonmagnetic metal attached to NiFe. Therefore, we confirmed that the magnetic rectification effect was negligible and that the inverse spin-Hall signal predominated. The SiO₂ inserted between NiFe and Cu effectively suppressed the STT generated by the alternating SC in Cu, whereas the SiO₂ inserted between NiFe and Pt eliminated the STT generated by the alternating SC in Pt. From the numerical result of the depth profile of the RSAW amplitude calculated using the finite-element method (FEM), we confirmed that the distribution of the RSAW amplitude barely changed when 20-nm-thick dielectric SiO₂ was inserted between the metallic layers. Moreover, as shown in Appendix A, we found that the gradient of the vorticity existed in the whole trilayer film. Indeed, we have also confirmed that a SWR can be excited in 20-nm-thick Ni via magnetoelastic coupling with a 1.85-GHz RSAW even when the Ni film is covered by semiconductor Si with a thickness of 400 nm, which is thicker than the total thickness of the Pt/NiFe/Cu trilayer [16]. The result suggests that the RSAW with a frequency of 1.85 GHz is not eliminated within 400 nm from the film surface. J_s^{SVC} can therefore be generated both in Cu and in Pt via SVC.

IV. EXPERIMENTAL RESULTS

Figure 2(a-2) is a color plot of the reduced microwave absorption ΔP^{norm} in the Pt/NiFe/Cu trilayer. The results are plotted in the external magnetic field versus the frequency plane. The reduced microwave absorption $\Delta P^{\text{norm}}(f, H)$ is

given by [5,16,17]

$$\Delta P^{\text{norm}}(f, H) = \frac{|\mathbf{P}_{21}(f, H) - \mathbf{P}_{21}(f, H_{\text{ref}})|}{P_{21}(f_{\text{SAW}}, H_{\text{ref}})}. \quad (6)$$

Here, $\mathbf{P}_{21}(f, H)$ is the complex power of the transmitted microwave calculated from S_{21} at a given frequency under an external magnetic field, and $\mathbf{P}_{21}(f, H_{\text{ref}})$ represents a reference signal at the given frequency under a fixed magnetic field ($\mu_0 H_{\text{ref}} = 20$ mT) at which the microwave attenuation owing to SWR is not observed at frequencies ranging from 1.5 to 2.0 GHz. The field-independent signal can therefore be removed by subtracting $\mathbf{P}_{21}(f, H_{\text{ref}})$ from $\mathbf{P}_{21}(f, H)$.

As shown in Fig. 2(a-2), the microwave absorption was maximized at 1.85 GHz under a 4.7-mT magnetic field. Figure 2(a-3) plots the microwave transmission at 20 mT as a function of frequency. The microwave absorption was largest at 1.85 GHz, the fundamental frequency of a RSAW propagating through the trilayer between the IDTs. Moreover, as indicated by dotted lines in Fig. 2(a-2), the microwave absorption was clearly strongest when both the microwave frequency and external magnetic field were matched to those of the dispersion relation of MSBVW excited in NiFe [18], given by

$$f = \frac{\gamma}{2\pi} \sqrt{|\mu_0 H| \left(|\mu_0 H| + \mu_0 M_s \frac{1 - e^{-kd_{\text{NiFe}}}}{kd_{\text{NiFe}}} \right)}, \quad (7)$$

where M_s , γ , and d_{NiFe} are the saturation magnetization of NiFe, the gyromagnetic ratio, and NiFe thickness, respectively. This result confirms that the MSBVW in NiFe was excited by injecting a RSAW into the trilayer.

Figures 2(a-4) and 2(a-5) plot ΔP^{norm} and the Hall voltage, respectively, as a function of the magnetic field at the fundamental frequency f_{SAW} (1.85 GHz), at which the RSAW is most efficiently injected into the trilayer. Comparing Figs. 2(a-4) and 2(a-5), we find that the absolute value of the Hall voltage was maximized in the positive and negative magnetic fields inducing the largest microwave absorption. This result confirms the spin-pumping effect of MSBVW excitation.

As shown in Figs. 2(d-2) and 2(d-4), the microwave absorption owing to the MSBVW excitation was absent when the alternating SC in Cu was blocked by the insulation of SiO₂. The result suggests that we can neglect the SWR caused by the alternating SC in Pt and/or the magnetoelastic [19] and Barnett effects in NiFe [17]. The insertion of the 20-nm-thick SiO₂ between NiFe and Pt doubles the peak value of ΔP^{norm} . It is noted that the peak value is inversely proportional to the effective Gilbert damping constant of the NiFe. Indeed, as shown later, the effective Gilbert damping constant of the NiFe/Pt bilayer is twice as large as the case in the NiFe monolayer. This is attributed to the relaxation of the spin angular momentum in the Pt via the spin-pumping effect. From these results, we can expect that the insertion of the SiO₂ thin film does not alter the mechanical coupling between the metallic stack and the LiNbO₃ substrate significantly.

To evaluate the strength of direct SC from the Hall voltage, we must consider the ISHE in both Pt and Cu because both metals are directly attached to NiFe, in which the MSBVW is excited. The Hall voltage associated with the ISHE in Cu can

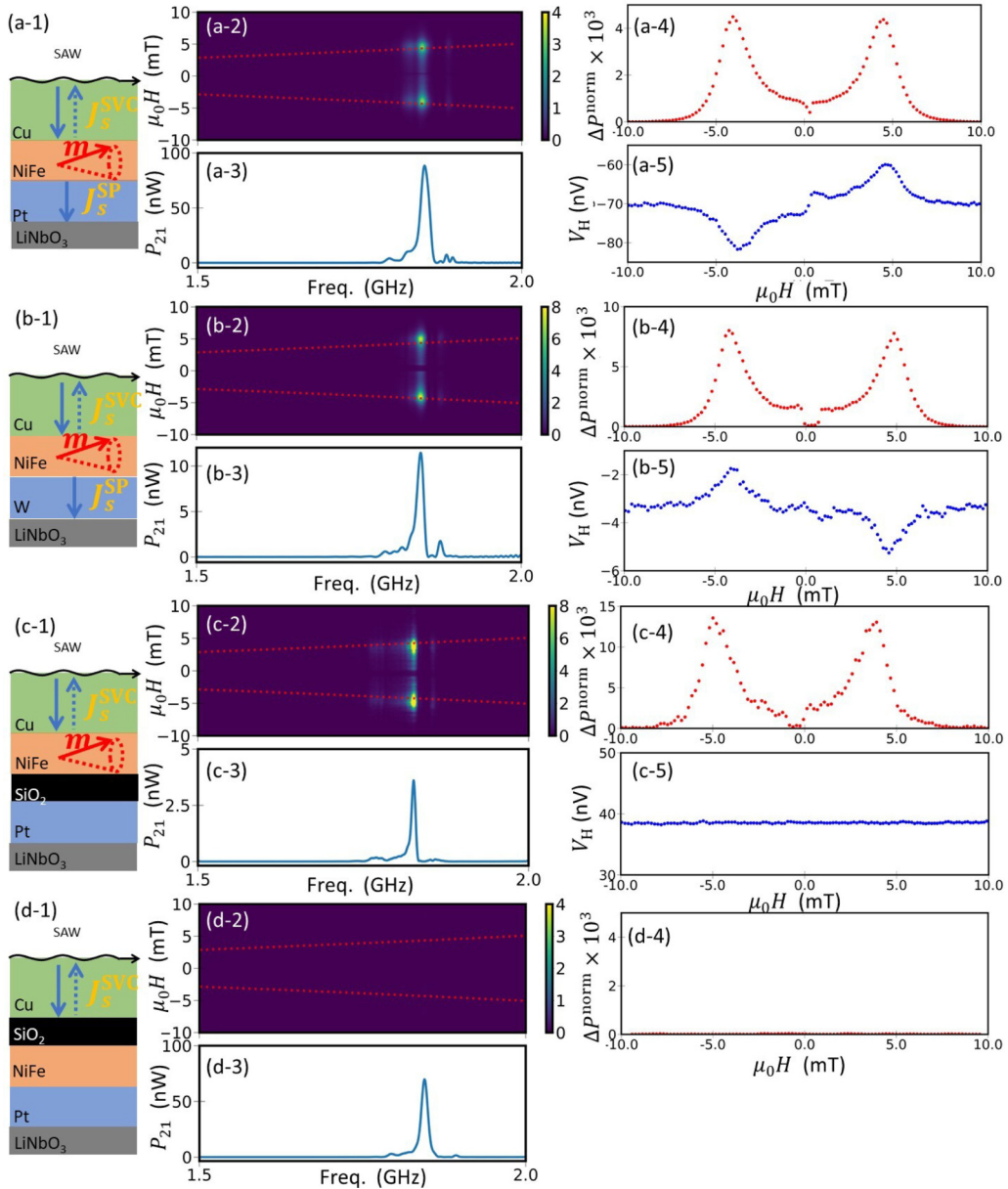


FIG. 2. (a-1)–(d-1) Schematic geometries of SWR excitation caused by J_s^{SVC} and consequent J_s^{SP} generation via the spin-pumping effect. Experimental results of RSAW-induced spin pumping in (a) Pt(10)/NiFe(20)/Cu(200), (b) W(10)/NiFe(20)/Cu(200), (c) Pt(10)/SiO₂(20)/NiFe/Cu(200), and (d) Pt(10)/NiFe(20)/SiO₂(20)/Cu(200). (a-2)–(d-2) Color plots of microwave absorption in the external field versus the frequency plane. (a-3)–(d-3) P_{21} at 20 mT as a function of frequency. (a-4)–(d-4) Microwave absorptions and (a-5)–(c-5) Hall voltages measured at each fundamental frequency of the RSAW.

be separately evaluated in the Pt/SiO₂/NiFe/Cu structure, which blocks the direct SC pumped from NiFe by the inserted SiO₂ and hence eliminates the Hall voltage associated with the ISHE in Pt. As shown in Fig. 2(c-5), the Hall voltage associated with the ISHE in Cu was negligibly small owing to the tiny spin-Hall angle of Cu [20].

Finally, we discuss how the magnetic rectification effect in NiFe influences the Hall voltage along the x axis. To evaluate the contribution of the magnetic rectification effect in NiFe, we examined the sign change in the Hall voltage when Pt was replaced with W. Recall that the spin-Hall angles of Pt and W are opposite in sign. The voltage induced by the magnetic rectification effect must be even with respect to the

spin-Hall angle of the adjacent nonmagnetic film. As shown in Fig. 2(b-5), the sign of the Hall voltage under a given magnetic field was reversed when Pt was replaced with W. Therefore, the Hall voltage developed in the trilayer injected with the RSAW was dominated by the ISHE in the Pt or W attached to NiFe.

V. ANALYTICAL MODEL FOR EVALUATING THE ALTERNATING SPIN CURRENT

In this section, we discuss the DC Hall voltage produced by the spin-pumping effect in the spatially nonuniform spin

wave mode. In the RSAW device, the side length of the trilayered square is shorter than the width of the IDT. Thus, the spread of the wave front of the RSAW is negligible. Moreover, the thickness of the NiFe layer is thinner than the exchange length. Consequently, the magnetization vector \mathbf{m} in the NiFe layer can be spatially varied only along the z axis. From the results of the input power dependence shown in Appendix B, the SWR was excited in a linear region. Consequently, we neglect nonlinear terms in our analytical model. The spatial and temporal evolution of the magnetization $\mathbf{m}(z, t)$ in an effective magnetic field \mathbf{H}_{eff} is generally described by the Landau-Lifshitz-Gilbert (LLG) equation [21],

$$\frac{d}{dt}\mathbf{m}(z, t) = -\gamma\mathbf{m}(z, t) \times \mu_0\mathbf{H}_{\text{eff}} + \frac{\alpha}{M_s}\mathbf{m}(z, t) \times \frac{d\mathbf{m}(z, t)}{dt}, \quad (8)$$

where α is the Gilbert damping constant. We suppose that \mathbf{H}_{eff} comprises an external magnetic field \mathbf{H}_{ex} , a demagnetizing field \mathbf{H}_{d} , and an effective magnetic field induced by STT \mathbf{H}_{st} as follows:

$$\mathbf{H}_{\text{eff}}(z, t) = \mathbf{H}_{\text{ex}} + \mathbf{H}_{\text{d}}(z, t) + \mathbf{H}_{\text{st}}(z, t), \quad (9)$$

where

$$\mathbf{H}_{\text{ex}} = \begin{pmatrix} 0 \\ 0 \\ H_{\text{ex}} \end{pmatrix}, \quad (10)$$

$$\mathbf{H}_{\text{d}}(z, t) = -\overleftrightarrow{\mathbf{N}}\mathbf{m}(z, t), \quad (11)$$

and

$$\mathbf{H}_{\text{st}}(z, t) = \frac{\hbar T J_s^{\text{SVC}}}{2e\mu_0 M_s^2 d_{\text{NiFe}}}\mathbf{m}(z, t) \times \boldsymbol{\sigma}(z, t), \quad (12)$$

where T , $\overleftrightarrow{\mathbf{N}}$, and e denote the spin transparency at the NiFe/Cu interface, the demagnetizing tensor, and the elementary charge, respectively. $\boldsymbol{\sigma}(z, t)$ is the spin polarization vector of J_s^{SVC} . Because d_{NiFe} is shorter than the exchange length of NiFe [22], the magnitude of H_{st} is independent of the y coordinate, although the amplitude of J_s^{SVC} decays within the spin diffusion length of the NiFe. In our analytical model, for simplicity, the in-plane demagnetizing field is assumed to be uniform because $kd_{\text{NiFe}} \ll 1$. As the rectangular surface area of the trilayer device is much larger than the NiFe thickness (20 nm), the demagnetizing tensor applicable for an infinite plane is assumed in Eq. (11). To solve Eq. (8), we consider a small precession limit of the magnetization $\mathbf{m}(z, t) = (m_x e^{i(\omega t - kz)}, m_y e^{i(\omega t - kz)}, M_s)$ around the equilibrium direction along the z axis and neglect the second-order contribution of the precession amplitude. The complex amplitudes of dynamic magnetization components m_x and m_y under the SWR excitation condition are respectively obtained as follows:

$$m_x = \frac{1}{(-i + \alpha)\gamma\mu_0 M_s + (2 + i\alpha)\alpha\omega} \frac{\gamma}{d_{\text{NiFe}}} \frac{\hbar}{2e} T J_s^{\text{SVC}}, \quad (13)$$

$$m_y = \frac{i(-i + \alpha)}{(-1 + i\alpha)\gamma\mu_0 M_s + (-2i + \alpha)\alpha\omega} \frac{\gamma}{d_{\text{NiFe}}} \frac{\hbar}{2e} T J_s^{\text{SVC}}. \quad (14)$$

According to general spin-pumping theory, the DC spin current J_s^{SP} pumped from a ferromagnet to an adjacent non-magnetic material is given by [15]

$$J_s^{\text{SP}} = \frac{\omega}{2\pi} \int_0^{2\pi/\omega} \frac{\hbar G_{\text{eff}}^{\uparrow\downarrow}}{4\pi} \frac{1}{M_s^2} \left\{ \text{Re}[\mathbf{m}] \times \frac{d}{dt} \text{Re}[\mathbf{m}] \right\} dt, \quad (15)$$

where $G_{\text{eff}}^{\uparrow\downarrow}$ is the real part of the effective spin-mixing conductance. The z dependence of the magnetization disappears after integration over one cycle of the time because the integral of Eq. (15) is invariant under the time-translation transformation of the integral. This analytical model suggests that the amplitude of the spatial and temporal J_s^{SVC} can be estimated by measuring J_s^{SP} via spin pumping from the SWR.

The direct electromotive force V_{H} resulting from the ISHE developed in the Pt of the Pt/NiFe/Cu trilayer is expressed as [15]

$$V_{\text{H}} = R_{\text{Pt}}\theta_{\text{SH}}\lambda_s \left(\frac{2e}{\hbar} \right) \tanh\left(\frac{d_{\text{Pt}}}{2\lambda_s} \right) J_s^{\text{SP}}. \quad (16)$$

Here, R_{Pt} , θ_{SH} , and d_{Pt} are the electrical resistance, spin-Hall angle, and thickness of the Pt layer, respectively. From Eqs. (13)–(16), we finally derive the relation between V_{H} and J_s^{SVC} as

$$V_{\text{H}} = R_{\text{Pt}}\theta_{\text{SH}}\lambda_s \left(\frac{2e}{\hbar} \right) \tanh\left(\frac{d_{\text{Pt}}}{2\lambda_s} \right) \frac{G_{\text{eff}}^{\uparrow\downarrow} \hbar \omega \gamma}{4\pi(1 + \alpha^2)\mu_0^2 M_s^4 d_{\text{NiFe}}^2} \times \left(T \frac{\hbar}{2e} J_s^{\text{SVC}} \right)^2. \quad (17)$$

Using Eq. (17), we can obtain the amplitude of J_s^{SVC} from the measured V_{H} . As seen in Eq. (17), the magnitude of V_{H} is inversely proportional to the square of d_{NiFe} . Namely, thinner NiFe is preferred to improve the detectable J_s^{SVC} from the V_{H} value. When d_{NiFe} is decreased from 20 nm to the spin diffusion length of NiFe (~ 4 nm) [23,24], the magnitude of V_{H} can be 25 times larger than in Figs. 2(a-5)–2(c-5). Conversely, thicker NiFe is better to observe the microwave absorption owing to the MSBVW excitation, as seen in Figs. 2(a-4)–2(d-4). In this study, we chose 20-nm-thick NiFe to satisfy the above conflicting requirements.

VI. EVALUATION OF THE ALTERNATING SPIN CURRENT GENERATED VIA SPIN-VORTICITY COUPLING

In this section, we quantitatively estimate the magnitude of J_s^{SVC} induced by SVC from the Hall voltage. Before evaluating the magnitude of J_s^{SVC} by Eq. (17), we require $G_{\text{eff}}^{\uparrow\downarrow}$ and T . Both parameters were determined by conventional VNA ferromagnetic resonance (FMR) measurements. From the Hall voltage, we then estimated the magnitude of J_s^{SVC} using the analytical model developed in Sec. V.

A. Spin-mixing conductance and spin transparency

The values of $G_{\text{eff}}^{\uparrow\downarrow}$ and T are generally evaluated from the change in the FMR linewidth when a nonmagnetic material contacts a resonating ferromagnet. Here, we evaluate $G_{\text{eff}}^{\uparrow\downarrow}$ and T at the Cu/NiFe and Pt/NiFe interfaces. For this purpose, we prepared microstrips of NiFe(20)/Pt(20), NiFe(20)/Cu(200),

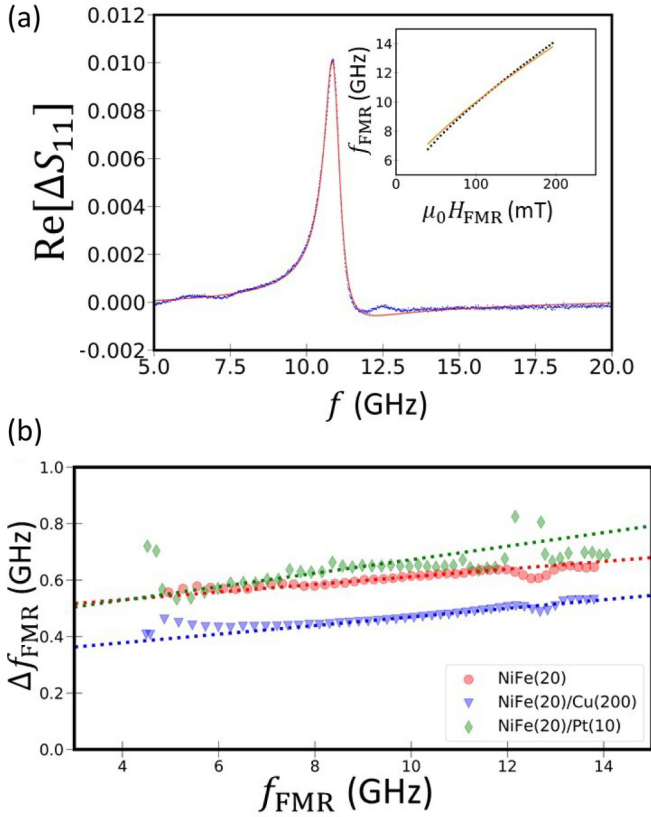


FIG. 3. (a) FMR spectrum of a 20-nm-thick NiFe film under a magnetic field of $\mu_0 H = 126$ mT. The solid line is the best-fit equation that combines the Lorentz and anti-Lorentz functions. The inset plots the FMR frequency as a function of external magnetic field (data points) and the best-fit Kittel equation for infinite ferromagnetic thin films (solid line). (b) Frequency linewidths of the FMR spectra as a function of FMR frequency in NiFe/Pt (green diamonds), NiFe/Cu (blue triangles), and NiFe (red circles). Dotted lines are the best-fit linear functions to the three data sets.

and NiFe(20) and electrically connected them to a coplanar wave guide (CPW) made of Ti(3)/Au(70) on a surface-oxidized Si substrate. The FMR spectrum was obtained by measuring the changing effective impedance while sweeping the external magnetic field along the longitudinal direction of the CPW. From the frequency dependence of the FMR linewidth, we evaluated the effective Gilbert damping constant.

Figure 3(a) represents a typical FMR spectrum of the NiFe(20) sample at $\mu_0 H = 126$ mT. ΔS_{11} is the background-subtracted S_{11} determined from the reference field measurements, $\mu_0 H_{\text{ref}} = 200$ mT. The FMR frequency and linewidth were evaluated by fitting the data to an equation combining the Lorentzian and anti-Lorentzian functions. As shown in the inset of Fig. 3(a), f_{FMR} versus $\mu_0 H_{\text{FMR}}$ was well fitted by the Kittel equation:

$$f_{\text{FMR}} = \frac{\gamma}{2\pi} \sqrt{|\mu_0 H_{\text{FMR}}| (|\mu_0 H_{\text{FMR}}| + \mu_0 M_s)}. \quad (18)$$

From the curve fitting, the saturation magnetization $\mu_0 M_s$ of the NiFe film was evaluated at 0.90 T.

Figure 3(b) plots the FMR linewidth versus FMR frequency in the NiFe/Pt, NiFe/Cu, and NiFe samples. The FMR linewidth Δf_{FMR} was generally given by [25]

$$\Delta f_{\text{FMR}} = \Delta f_0 + 2\alpha f_{\text{FMR}}, \quad (19)$$

where Δf_0 is the linewidth broadening induced by the inhomogeneous magnetic properties. Thus, the Gilbert damping constant can be evaluated from the gradient of the Δf_{FMR} versus f_{FMR} plot for each sample. Fitting the experimental results to Eq. (19), we estimated α as 0.0067, 0.012, and 0.0076 in the NiFe, NiFe/Pt, and NiFe/Cu samples, respectively.

According to spin-pumping theory [15], α is enlarged when a ferromagnetic material is attached to a nonmagnetic metal because the pumped spin angular momentum is relaxed via the SOI in the nonmagnetic metal. Thus, α depends on $G_{\text{eff}}^{\uparrow\downarrow}$ as follows [26]:

$$\alpha_{\text{NiFe/Pt(Cu)}} = \alpha_{\text{NiFe}} + G_{\text{eff}}^{\uparrow\downarrow} \frac{g\mu_B}{4\pi M_s d_{\text{NiFe}}}, \quad (20)$$

where g and μ_B are the g factor and Bohr magneton. α_{NiFe} and $\alpha_{\text{NiFe/Pt(Cu)}}$ are the Gilbert damping constant of the bare NiFe film and NiFe/Pt(Cu) film, respectively. To evaluate $G_{\text{eff}}^{\uparrow\downarrow}$, we compared the Gilbert damping constants with and without spin pumping. Finally, the $G_{\text{eff}}^{\uparrow\downarrow}$ values at the NiFe/Pt and NiFe/Cu interfaces were determined as 4.0 and 0.69 nm^{-2} , respectively. These values quantitatively agree with the previously reported spin-mixing conductance [27].

Assuming spin-Hall magnetoresistance theory, the spin transparency T at the NiFe/Cu interface was determined as [28,29]

$$T = \frac{G^{\uparrow\downarrow} \tanh\left(\frac{d_{\text{Cu}}}{2\lambda_s}\right)}{G^{\uparrow\downarrow} \coth\left(\frac{d_{\text{Cu}}}{\lambda_s}\right) + \frac{\sigma_{\text{Cu}} \hbar}{2e^2 \lambda_s}}, \quad (21)$$

where

$$G^{\uparrow\downarrow} = G_{\text{eff}}^{\uparrow\downarrow} \frac{\frac{\sigma_{\text{Cu}} \hbar}{2e^2 \lambda_s} \tanh\left(\frac{d_{\text{Cu}}}{\lambda_s}\right)}{\frac{\sigma_{\text{Cu}} \hbar}{2e^2 \lambda_s} \tanh\left(\frac{d_{\text{Cu}}}{\lambda_s}\right) - G_{\text{eff}}^{\uparrow\downarrow}} \quad (22)$$

and σ_{Cu} is the conductivity of Cu. $G^{\uparrow\downarrow}$ is the bare spin-mixing conductance, estimated by considering the spin-backflow effect in the effective spin-mixing conductance [30]. Inserting $G_{\text{eff}}^{\uparrow\downarrow}$ into Eqs. (21) and (22), T at the NiFe/Cu interface was calculated as 0.074.

B. Evaluation of alternating spin current from Hall voltage

Finally, we evaluated J_s^{SVC} from the Hall voltage. Fitting the Hall voltage spectrum [Fig. 2(a-5)] to a symmetric Lorentzian function, the electromotive force induced by the ISHE in Pt was evaluated at 12.0 nV. Inserting the Hall voltages measured in Pt/NiFe/Cu [Fig. 2(a-5)], the T and $G_{\text{eff}}^{\uparrow\downarrow}$ values evaluated at the NiFe/Pt interface, and the typical values of θ_{SH} and λ_s for Pt (0.03 and 8.0 nm, respectively) [31] into Eq. (17), J_s^{SVC} was calculated as 3.8×10^{11} A/m². The effective field of J_s^{SVC} driving the NiFe magnetization dynamics was calculated as $H_{\text{st}} = 0.6$ mT by Eq. (12). In a spin-torque FMR experiment in which the SWR was similarly excited by an alternating SC, the consequent direct SC emitted via spin pumping was determined to be $J_s^{\text{SP}} = C f G_{\text{eff}}^{\uparrow\downarrow} \hbar^2$.

Here, h is the effective radio-frequency field driving the magnetization precession, and C is a material-dependent parameter. In the conventional spin-pumping experiment for the NiFe/Pt bilayer film [32], the value of C is evaluated to be 6.2×10^{-33} J s/T, with $J_s^{\text{SP}} = 9.5 \times 10^5$ A/m², $G_{\text{eff}}^{\uparrow\downarrow} = 2 \times 10^{19}$ m⁻², $f = 8$ GHz, and $h = 0.55$ mT. In our case, the value of J_s^{SP} can be evaluated to be 8.5×10^3 A/m² from the experimentally measured V_H and Eq. (16). Using J_s^{SP} , $G_{\text{eff}}^{\uparrow\downarrow}$, and H_{st} , we estimated a similar C value of 8.8×10^{-34} J s/T. This comparable spin-pumping parameter C confirms that J_s^{SVC} was properly estimated by our analytical model.

Finally, we evaluate the conversion parameter of the angular momentum from lattice vorticity into electron spin ζ from the obtained amplitude of J_s^{SVC} and Eqs. (4)–(5). Recently, we succeeded in evaluating the amplitude of u_0 in the RSAW device by measuring the SWR excited with the Barnett effect [17]. The RSAW amplitude averaged along the film thickness was evaluated at 6.3 pm when a microwave with an amplitude of 5 dBm was applied to the IDT. Thus, we can expect the value to be 79 pm when the input power increases to 17 dBm. From the u_0 value, we obtain ζ of 2.6×10^6 , which is four orders of magnitude larger than that of liquid-mercury flow [2,3]. Theoretically, the conversion efficiency of the angular momentum from the lattice into electron spins becomes larger when the difference of the energy scales is smaller between lattice motion and spins. Consequently, the renormalization factor of the elastic system is much larger than that of the liquid-metal flow because the elastic motion of our setup is in the gigahertz range whereas the vorticity of the liquid-metal flow is in the kilohertz range.

VII. CONCLUSION

In this paper, we evaluated the alternating SC generated in a Cu thin film via SVC of the RSAW. Spin pumping in the Pt/NiFe/Cu trilayer converts the alternating SC into the direct SC, which is proportional to the squared amplitude of the alternating SC and can be electrically detected by ISHE. Comparing the ISHE signals of the W/NiFe/Cu, Pt/SiO₂/NiFe/Cu, and Pt/NiFe/SiO₂/Cu systems, we confirmed that the SWR was excited by the alternating SC generated in the Cu layer. When spin pumping converted the alternating SC to direct SC, a Hall voltage appeared in the Pt layer. Using our analytical relation between the alternating and direct SCs, we estimated the alternating SC in the Cu layer to be 3.8×10^{11} A/m² under SAW excitation by an electric power of 17 dBm. From the SC amplitude, we found that the renormalization factor ζ of the RSAW-driven SVC in the Cu film can be much larger than the SVC in a liquid-Hg flow. Namely, the elastic vorticity of SAW is suitable for the SC generation via SVC. To further understand the microscopic mechanism of the SVC, the material dependence of ζ should be investigated; especially, the influence of the spin-orbit coupling on the magnitude of SVC is important to discuss the coupling between macroscopic angular momentum and microscopic spin angular momentum.

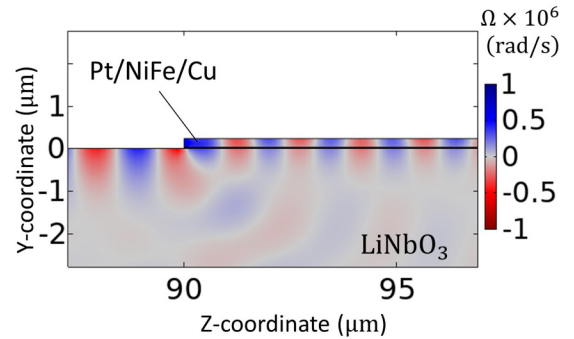


FIG. 4. Color plot of RSAW vorticity calculated for the Pt(10)/NiFe(20)/Cu(200) trilayer on the LiNbO₃ substrate.

ACKNOWLEDGMENTS

The authors would like to thank J. Fujimoto for his valuable discussions. This work was partially supported by JSPS KAKENHI Grant No. JP18H03867 and JST CREST Grant No. JPMJCR19J4, Japan. G.O. is supported by JSPS through a research fellowship for young scientists (Grant No. 18J20062).

APPENDIX A: FEM CALCULATION OF SAW

In Sec. IV, we compared ΔP^{norm} values between Pt/NiFe/Cu and Pt/SiO₂/NiFe/Cu to evaluate the magnitude of SWR owing to a SC generated in the Pt layer via SVC. In the comparison, we assumed that the intensity distribution of the vorticity in Pt/NiFe/Cu bilayer was not changed by inserting 20-nm-thick SiO₂ between Pt and NiFe. To confirm the assumption, we examined the distribution of the RSAW vorticity numerically using the FEM with the COMSOL MULTIPHYSICS software package [33]. The geometry and material parameters used for the FEM calculation were identical to the experimental conditions. A perfectly matched layer was assumed in the bottom layer to prevent wave reflection. One of the IDTs was connected to a microwave source with a power of -5 dBm, and another IDT was terminated with 50Ω impedance. We compared the distribution of the RSAW vorticity between two

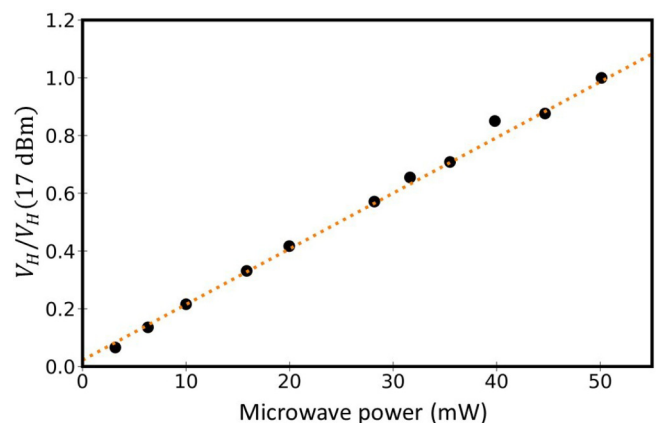


FIG. 5. Microwave power dependence of reduced V_H by the reference value at 17 dBm. The dotted line shows the result of the best fit with a linear function.

layer configurations consisting of Pt(10)/NiFe(20)/Cu(200) and Pt(10)/SiO₂(20)/NiFe(20)/Cu(200). Figure 4 shows a color plot of RSAW vorticity at the fundamental frequency for Pt(10)/NiFe(20)/Cu(200). The polarity of the vorticity changes along the z axis with a period of the RSAW wavelength, which is consistent with the analytical solution in Eq. (3). As shown in Fig. 4, the RSAW vorticity exists throughout the trilayer. We confirmed that the insertion of 20-nm-thick SiO₂ between the Pt and NiFe layers showed only an 8% decrease of the vorticity at the NiFe/Cu interface. The numerical result is consistent with the experimental result that the peak magnitude of ΔP^{norm} is not decreased with the insertion of a SiO₂ layer.

APPENDIX B: POWER DEPENDENCE OF THE HALL VOLTAGE

Figure 5 shows the reduced Hall voltage V_H by the reference value at 17 dBm as a function of input power. The amplitude of u_0 is proportional to the square root of the microwave power used to excite the RSAW. From Eqs. (5) and (17), therefore, the measured V_H is also proportional to the microwave power. Indeed, as shown in Fig. 5, the value of V_H increases linearly with the microwave power up to 50 mW. The result suggests that our experiment is in the linear responding regime, and consequently, we can linearize the LLG equation as shown in Sec. V.

-
- [1] M. Matsuo, J. Ieda, K. Harii, E. Saitoh, and S. Maekawa, *Phys. Rev. B* **87**, 180402(R) (2013).
- [2] M. Matsuo, Y. Ohnuma, and S. Maekawa, *Phys. Rev. B* **96**, 020401(R) (2017).
- [3] R. Takahashi, M. Matsuo, M. Ono, K. Harii, H. Chudo, S. Okayasu, J. Ieda, S. Takahashi, S. Maekawa, and E. Saitoh, *Nat. Phys.* **12**, 52 (2015)
- [4] J. Ieda, M. Matsuo, and S. Maekawa, *Solid State Commun.* **198**, 52 (2014).
- [5] D. Kobayashi, T. Yoshikawa, M. Matsuo, R. Iguchi, S. Maekawa, E. Saitoh, and Y. Nozaki, *Phys. Rev. Lett.* **119**, 077202 (2017)
- [6] E. Saito, M. Ueda, H. Miyajima, and G. Tatara, *Appl. Phys. Lett.* **88**, 182509 (2006)
- [7] S. O. Valenzuela and M. Tinkham, *Nature (London)* **442**, 176 (2006).
- [8] H. Zhao, E. J. Loren, H. M. van Driel, and A. L. Smirl, *Phys. Rev. Lett.* **96**, 246601 (2006).
- [9] T. Kimura, Y. Otani, T. Sato, S. Takahashi, and S. Maekawa, *Phys. Rev. Lett.* **98**, 156601 (2007).
- [10] S. Takahashi and S. Maekawa, *J. Phys. Soc. Jpn.* **77**, 031009 (2008).
- [11] Y. Tserkovnyak, A. Brataas, and G. E. W. Bauer, *Phys. Rev. B* **66**, 224403 (2002).
- [12] Y. Kajiwara, K. Harii, S. Takahashi, J. Ohe, K. Uchida, M. Mizuguchi, H. Umezawa, H. Kawai, K. Ando, K. Takanashi, S. Maekawa, and E. Saitoh, *Nature (London)* **464**, 262 (2010).
- [13] O. Mosendz, J. E. Pearson, F. Y. Fradin, G. E. W. Bauer, S. D. Bader, and A. Hoffmann, *Phys. Rev. Lett.* **104**, 046601 (2010).
- [14] F. W. Hehl and W. T. Ni, *Phys. Rev. D* **42**, 2045 (1990).
- [15] K. Ando, S. Takahashi, J. Ieda, Y. Kajiwara, H. Nakayama, T. Yoshino, K. Harii, Y. Fujikawa, M. Matsuo, S. Maekawa, and E. Saitoh, *J. Appl. Phys.* **109**, 103913 (2011).
- [16] S. Tateno and Y. Nozaki, *Phys. Rev. Appl.* **13**, 034074 (2020).
- [17] Y. Kurimune, M. Matsuo, and Y. Nozaki, *Phys. Rev. Lett.* **124**, 217205 (2020).
- [18] D. D. Stancil and Prabhakar, *Spin Waves: Theory and Application* (Springer, New York, 2009).
- [19] M. Weiler, L. Dreher, C. Heeg, H. Huebl, R. Gross, M. S. Brandt, and S. T. B. Goennenwein, *Phys. Rev. Lett.* **106**, 117601 (2011).
- [20] H. L. Wang, C. H. Du, Y. Pu, R. Adur, P. C. Hammel, and F. Y. Yang, *Phys. Rev. Lett.* **112**, 197201 (2014).
- [21] L. Liu, T. Moriyama, D. C. Ralph, and R. A. Buhrman, *Phys. Rev. Lett.* **106**, 036601 (2011).
- [22] J. Grafe, G. Schutz, and E. J. Goering, *J. Magn. Magn. Mater.* **419**, 517 (2016).
- [23] T. Kimura, J. Hamrle, and Y. Otani, *Phys. Rev. B* **72**, 014461 (2005).
- [24] G. Zahnd, L. Vila, V. T. Pham, M. Cosset-Cheneau, W. Lim, A. Brenac, P. Laczkowski, A. Marty, and J. P. Attané, *Phys. Rev. B* **98**, 174414 (2018).
- [25] M. Farle, *Rep. Prog. Phys.* **61**, 755 (1998).
- [26] Y. Tserkovnyak, A. Brataas, G. E. W. Bauer, and B. I. Halperin, *Rev. Mod. Phys.* **77**, 1375 (2005).
- [27] G. Okano, M. Matsuo, Y. Ohnuma, S. Maekawa, and Y. Nozaki, *Phys. Rev. Lett.* **122**, 217701 (2019).
- [28] Y.-T. Chen, S. Takahashi, H. Nakayama, M. Althammer, S. T. B. Goennenwein, E. Saitoh, and G. E. W. Bauer, *Phys. Rev. B* **87**, 144411 (2013).
- [29] W. Zhang, W. Han, X. Jiang, S. Yang, and S. P. Parkin, *Nat. Phys.* **11**, 496 (2015).
- [30] H. J. Jiao and G. E. W. Bauer, *Phys. Rev. Lett.* **110**, 217602 (2013).
- [31] X. Tao, Q. Liu, B. Miao, R. Yu, Z. Feng, L. Sun, B. You, J. Du, K. Chen, S. Zhang, L. Zhang, Z. Yuan, D. Wu, and H. Ding, *Sci. Adv.* **4**, eaat1670 (2018).
- [32] Y. Wang, P. Deorani, X. Qiu, J. H. Kwon, and H. Yang, *Appl. Phys. Lett.* **105**, 152412 (2014).
- [33] COMSOL MULTIPHYSICS, <https://www.comsol.com/>.